

Evolution of Interorbital Superconductor to Intraorbital Spin-Density Wave in Layered Ruthenates

Austin W. Lindquist,¹ Jonathan Clepkens,¹ and Hae-Young Kee^{1,2,*}

¹*Department of Physics and Center for Quantum Materials, University of Toronto, 60 St. George St., Toronto, Ontario, M5S 1A7, Canada*
²*Canadian Institute for Advanced Research, Toronto, Ontario, M5G 1Z8, Canada*

The ruthenate family of layered perovskites has been a topic of intense interest with much work dedicated to understanding the superconducting state of the single layer, Sr_2RuO_4 . Another longstanding puzzle is the lack of superconductivity in its sister compound, $\text{Sr}_3\text{Ru}_2\text{O}_7$, which constrains the possible superconducting mechanisms of Sr_2RuO_4 . Here we address a microscopic mechanism that unifies superconducting and spin-density wave order in this family of materials. Beginning from a model of Sr_2RuO_4 featuring intraband pseudospin-singlet superconductivity originating from interorbital spin-triplet pairing via Hund's and spin-orbit couplings, the addition of bilayer coupling and staggered rotations of the oxygen octahedra are investigated. We find that the bilayer coupling alone enhances superconductivity, while staggered rotations destroy interorbital superconductivity, leaving a paramagnetic metal. The magnetic field then shifts van Hove singularities near the Fermi level, allowing intraorbital SDW order to form in the bilayer. Our theory predicts that bilayer $\text{Sr}_3\text{Ru}_2\text{O}_7$ without staggered rotations exhibits interorbital superconductivity with a possibly higher transition temperature.

Introduction – Multiorbital systems in which the low-energy behavior is affected by the various orbitals provide an ideal setup for the formation of rich electronic phases. One notable example is the family of layered perovskites, $\text{Sr}_{n+1}\text{Ru}_n\text{O}_{3n+1}$. Much attention has been paid to the single layer material, Sr_2RuO_4 (214), which displays superconductivity (SC) at low temperatures [1–4]. However, despite intense studies, the nature of the superconducting state still remains a topic of debate [4, 5]. Interest in the bilayer material, $\text{Sr}_3\text{Ru}_2\text{O}_7$ (327), grew after significant anisotropy in the resistivity, signaling an electronic nematic phase was reported [6–12]. More recently, a resistivity linear in temperature [13], as well as spin-density wave (SDW) order were found to occur at low temperatures at field values coinciding with the presumed nematic phase, bounded by metamagnetic transitions [14, 15].

One of the longstanding puzzles in this family is the lack of SC in 327, which constrains the possible superconducting mechanisms of 214. The similarity of the two materials means that a model of the single layer should be able to explain the lack of SC in the bilayer and its sensitivity to the differences between the two. The two notable differences introduced by the inclusion of the second layer in 327 are (1) the bilayer coupling and (2) the staggered rotations of the oxygen octahedra. The observation of SDW order in the presence of a magnetic field in 327 suggests a delicate competition between SC and SDW in these two sister compounds, calling for a unified picture.

Here, we address the microscopic mechanism of the evolution from SC in 214 to the SC is destroyed by the bilayer coupling or SDW order in 327. We show that the absence of SC in 327 supports interorbital pairing in 214 which is sensitive to orbital mixing via SOC. Using the same parameter set for the Kanamori Hamiltonian, we find interorbital spin-triplet SC is destroyed by the staggered rotations of the octahedra, and intraorbital SDW order emerges under a magnetic field in 327. Further, we predict that ideal bilayer 327 without staggered rotations of the octahedra,

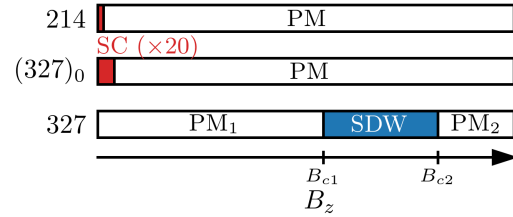


Figure 1. Phase diagram of the single-layer, 214, ideal bilayer (no staggered rotations of octahedra), $(327)_0$, and real bilayer, 327. The single layer and ideal bilayer both feature superconducting regions at small fields, with the ideal bilayer having an expanded superconducting region. Both regions are expanded by a factor of 20 to more clearly show their relative sizes. In 327, SC is destroyed by rotations of the octahedra, and SDW order exists at finite field values between B_{c1} and B_{c2} . The values of B_{c1} and B_{c2} and other relevant parameters are given in the main text. The two distinct paramagnetic regions surrounding the SDW order, labeled PM_1 and PM_2 , represent the low- and high-moment regions, respectively.

denoted $(327)_0$ displays interorbital SC with a transition temperature possibly higher than 214, as shown in Fig. 1, the phase diagram of these systems in a field.

Microscopic theory – Sr_2RuO_4 was once thought to be a leading candidate for $p + ip$ spin-triplet SC [16, 17]. However, recent NMR data showing a drop in the Knight shift below the superconducting transition temperature seems to rule out odd-parity spin-triplet pairing [18, 19]. While p -wave states may not explain the Knight shift reduction, spin-triplet proposals still remain a possibility with even-parity interorbital spin-triplet states [20–27]. This pairing in the orbital basis is spin-triplet, however, it appears as a pseudospin-singlet in the band basis due to the SOC. The interorbital nature of the pairing means that significant band degeneracy near the Fermi level is required for the pairing [28, 29]. Alternatively, when the SOC and band separation are comparable in energy, the SOC stabilizes the

interorbital pairing via mixing of orbitals and spin under a reasonable strength of Hund's coupling [20, 24, 26, 27, 30–33].

We adopt the Kanamori Hamiltonian, well known for multiorbital systems, to investigate competition between SC pairing and SDW order in 214, (327)₀, and 327. In multiorbital systems, the distinction between intraorbital, interorbital-singlet, and interorbital-triplet pairings must all be considered. Taking into account the attractive interaction occurring for interorbital SC pairings and intraorbital SDW ordering, the effective Hamiltonian is found as,

$$\begin{aligned} \frac{H_{\text{eff}}}{N} = & 2(U - 3J_H) \sum_{a \neq b} \hat{\Delta}_{a/b}^\dagger \cdot \hat{\Delta}_{a/b} \\ & - 2U \sum_{\mathbf{a}} \hat{m}_{\mathbf{a}}^a \cdot \hat{m}_{-\mathbf{a}}^a - J_H \sum_{\mathbf{a} \neq \mathbf{b}} \hat{m}_{\mathbf{a}}^a \cdot \hat{m}_{-\mathbf{b}}^b, \end{aligned} \quad (1)$$

where the orbital-singlet, spin-triplet, superconducting order parameter, $\hat{\Delta}_{a/b}^\dagger$, is written as,

$$\hat{\Delta}_{a/b}^\dagger = \frac{1}{4N} \sum_{\mathbf{k}} [i\hat{\sigma}^y \hat{\sigma}^l]_{\sigma\sigma'} (c_{\mathbf{k},\sigma}^{a\dagger} c_{-\mathbf{k},\sigma'}^{b\dagger} - c_{\mathbf{k},\sigma}^{b\dagger} c_{-\mathbf{k},\sigma'}^{a\dagger}), \quad (2)$$

with $l = x, y, z$ and $a \neq b$ represents the sum over the unique pairs of orbital indices in (yz, xz, xy) . The electron operator $c_{\mathbf{k},\sigma}^{a\dagger}$ creates an electron in orbital a with spin σ . The intraorbital SDW order parameter, $\hat{m}_{\mathbf{a}}^a$, is given by,

$$\hat{m}_{\mathbf{a}}^a = \frac{1}{2N} \sum_{\mathbf{k}} c_{\mathbf{k}+\mathbf{a}/2,\sigma}^{a\dagger} [\hat{\sigma}]_{\sigma,\sigma'} c_{\mathbf{k}-\mathbf{a}/2,\sigma'}. \quad (3)$$

Throughout this work we fix the values of U and J_H with values of $U = 0.8047$ and $J_H = 0.4287$ such that $U - 3J_H = -0.4814$, all in units of $2t_x^{xz} = 1$ as shown in Table I of the supplementary material (SM). While the condition of $U - 3J_H < 0$ may not be realistic for bare electron interactions, studies using dynamical mean-field theory found the interorbital triplet when $U - 3J_H > 0$ [21–23], suggesting that such a condition is not required in low energy physics. Tight-binding (TB) parameters obtained from density functional theory (DFT) calculations are given in the SM. The SC pairing itself is insensitive to the choice of TB parameters, however, the symmetry of the SC pairing state depends on the details as shown in Ref. 27, but the evolution of SC to SDW from 214 to 327 is robust, independent of SC pairing symmetry. In the next section, we explore the effects of orbital-dependent bilayer coupling on SC. We also examine hopping terms from staggered rotations, and show that this is responsible for the lack of SC in 327.

Evolution of SC – The structure of 327 closely resembles that of two stacked layers of 214. To construct a TB model of the bilayer beginning from the single layer, interlayer hopping terms must be added, which we refer to collectively as the bilayer coupling. In addition to the bilayer coupling, intralayer hopping terms which are already present may be modified, and additional terms added due to the staggered rotations of the octahedra observed in the bilayer but not the single layer.

Self-consistent mean-field (MF) calculations are performed for the TB models of the single layer, 214, the ideal bilayer, (327)₀, and the bilayer, 327, where (327)₀ uses the TB parameters from the single layer with bilayer coupling added. The phase diagram in a magnetic field perpendicular to the layers is shown in Fig. 1, where areas of finite SC are shown in red. The model of 214 features SC, which is increased when bilayer coupling is added in (327)₀. The addition of staggered rotations in 327 destroys all of the SC regions, which are replaced by a paramagnet (PM).

To understand why SC is enhanced in (327)₀, let's consider the effect of the interlayer hopping in a two orbital model. Interlayer hopping terms depend on the orbitals and are largest for yz to yz and xz to xz hopping, while it is minimal between the xy orbitals. A two-orbital model of xz (or yz) and xy gives insight into the effects of bilayer coupling. We use the basis $\Psi_k^\dagger = (\psi_k^\dagger, \mathcal{T} \psi_k^T \mathcal{T}^{-1})$ where \mathcal{T} represents time-reversal, and $\psi_k^\dagger = (c_{k,1,\uparrow}^{xz\dagger}, c_{k,1,\downarrow}^{xz\dagger}, c_{k,1,\uparrow}^{xy\dagger}, c_{k,1,\downarrow}^{xy\dagger}, c_{k,2,\uparrow}^{xz\dagger}, c_{k,2,\downarrow}^{xz\dagger}, c_{k,2,\uparrow}^{xy\dagger}, c_{k,2,\downarrow}^{xy\dagger})$, where the top and bottom layers are represented by the subscript 1 and 2, respectively. The kinetic and SOC parts of the Hamiltonian are then given by,

$$\begin{aligned} H_k = & \xi_k^+ \rho_3 \eta_0 \tau_0 \sigma_0 + \xi_k^- \rho_3 \eta_0 \tau_3 \sigma_0 + \lambda \rho_3 \eta_0 \tau_2 \sigma_1 \\ & + \frac{1}{2} t_\perp \rho_3 \eta_1 (\tau_0 + \tau_3) \sigma_0, \end{aligned} \quad (4)$$

where η , τ , σ , and ρ are Pauli matrices representing the layer, orbital, spin, and particle-hole bases, respectively. The orbital dispersions in the xz and xy orbitals are represented by $\xi_k^{xz/xy} = \xi_k^+ \pm \xi_k^-$ and left in this general form here. Details of these dispersions used in the full three-orbital model can be found in the SM. The SOC is given by λ , and the interlayer hopping exists only in orbital xz , given by t_\perp .

The interorbital-singlet spin-triplet pairing, $\Delta_x^{xz/xy}$, with a d -vector in the x -direction is written as,

$$H_{\text{SC}} = \Delta_x^{xz/xy} \rho_1 \eta_0 \tau_2 \sigma_1. \quad (5)$$

Transforming H_{SC} to the band basis, i.e., the basis in which H_k is diagonal, it is clear how intraband pairing forms, and how the various terms affect the gap size. Doing such a transformation provides the magnitude of the intraband gaps in the two bands;

$$|\Delta_{\text{band}}^\pm| = \frac{2\lambda \Delta_x^{xz/xy}}{\sqrt{(\xi_k^- \pm \frac{1}{2} t_\perp)^2 + 4\lambda^2}}. \quad (6)$$

This shows first that SOC is responsible for the formation of the intraband gap, consistent with previous works when $t_\perp = 0$ [26, 27]. Second, it relates the interorbital SC pairing, $\Delta_x^{xz/xy}$, to the pairing on the band, Δ_{band} , where the pairing on the band is affected by the band dispersion $\sqrt{(\xi_k^- + \frac{1}{2} t_\perp)^2 + 4\lambda^2}$ or $\sqrt{(\xi_k^- - \frac{1}{2} t_\perp)^2 + 4\lambda^2}$. The pairing on one of the bands is increased by the bilayer coupling, t_\perp , if the degeneracy of the bands is increased. Therefore, when the bilayer coupling brings two bands closer together

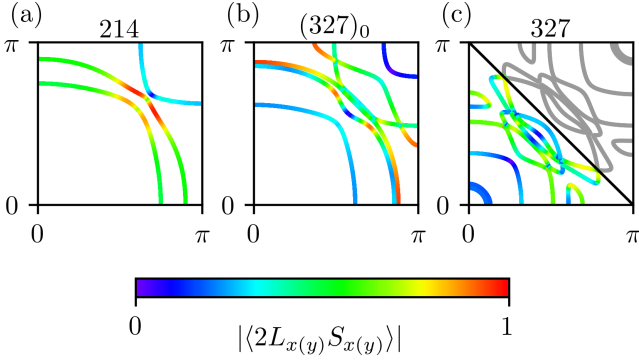


Figure 2. Character of the mixing of orbitals and spins at the Fermi level at zero field, measured by $\langle 2L_{x(y)}S_{x(y)} \rangle$, for TB models of (a) 214, (b) the bilayer with no rotations, $(327)_0$, and (c) 327. Larger mixing favors interorbital SC [20]. The areas where these states mix most are shown in red, where pairing will be strongest. Introducing bilayer coupling that increase the band degeneracy leads to more areas where SC can form, as shown for $(327)_0$. This is not the case when staggered rotations are included in 327 consistent with self-consistent MF results shown in Fig. 1.

near the Fermi level, the resulting bands feature a more significant mixture of the two orbitals with appropriate spin character via SOC, and thus are more ideal for interorbital SC to form.

The effect of the bilayer coupling on the orbital and spin mixing, shown for 214 in Figs. 2(a) and (b), is another way to understand the effect on interorbital SC pairing. This displays the trend of the orbital and spin mixing via SOC, measured by $\langle 2L_x S_x \rangle$ or $\langle 2L_y S_y \rangle$, which is favorable for either $\Delta_x^{xz/xy}$ or $\Delta_y^{yz/xy}$ within each of the bands at the Fermi level, where red areas are the most mixed, ideal for SC. Note that not all bands exhibit the increase in such mixing due to the bilayer, i.e., the bilayer can in principle decrease the band degeneracy, which works against the SC. For the 214 TB model though, we found that it works in favor of the SC. While the pairing in the orbital basis has no momentum dependence, higher-angular momentum pairing can be revealed in the band basis due to momentum-dependent SOC or a combination of dispersion terms and SOC [26, 27]. This allows for gap nodes and complex multi-component order parameters, beyond the current study, however, the results presented here on the evolution from SC to SDW is independent of the type of pairing symmetry.

Next, we consider the effect of the staggered rotations present in 327. While the bilayer coupling may bring band energies closer together and increase degeneracy, orbital hybridization is detrimental to the formation of interorbital-singlet spin-triplet SC [26, 30]. The hybridization from staggered rotations in 327 is included in Fig. 2(c), showing that all of the areas of maximum mixing in the single layer and ideal bilayer models have disappeared, destroying SC. This is consistent with the phase diagram of 327 in Fig. 1, obtained by self-consistent MF calculations. To compare, we also consider intraorbital SC and show that, following

an increase in the DOS, intraorbital SC is enhanced by both the bilayer coupling and staggered rotations, shown in the SM. This contrasts with experimental observations, which further supports the interorbital SC in these systems.

Spin-density wave ordering – In addition to interorbital SC, the Kanamori Hamiltonian also provides the intraorbital SDW instability. Specifically, with the Hubbard interaction, SDW order appears when an appropriate nesting vector exists. Previous studies on the magnetic susceptibility of 214 have found strong nesting from an intraband nesting vector around $\mathbf{q} \approx (\pm\frac{\pi}{2}, \pm\pi)$ to $(\pm\frac{2\pi}{3}, \pm\pi)$ depending on TB parameters [23, 34]. However, no SDW order is found in unstrained 214 at low temperatures, suggesting that this nesting is not sufficient for SDW order. Similar nesting is present in 327, with nesting vector values of $\mathbf{q} \approx (\pm\frac{\pi}{2}, 0)$ to $(\pm\frac{\pi}{3}, 0)$ due to the unit cell doubling. In addition to this vector, there also exists the same vector rotated by $\frac{\pi}{2}$ (i.e., along the y -direction instead). As in the case of 214, this nesting alone is not sufficient, as no SDW order forms at zero field. It was shown that the SDW order is suppressed by SOC in 327 by reducing the nesting [35], but the importance of SOC in this material has been recognized in explaining the dependence of the metamagnetic transition on the orientation of the field [35]. Additionally, experiments show a strong dependence of the formation of SDW order on the orientation of the field [14].

Although the nesting in 327 at zero field is not enough for SDW order to form, the presence of a van Hove singularity (vHS) was experimentally identified in the bilayer in the presence of a field [36], and it was suggested that the metamagnetic and nematic transitions are driven by the vHS [37–42]. We therefore consider the effect of the nesting and vHS together on the formation of SDW order in 327. Analysis of the 327 TB model obtained via DFT reveals a peak in the DOS just below the Fermi level. Introducing a magnetic field splits the peak in two, bringing one towards the Fermi level, leading to a significant change in the magnetization once the peak reaches the Fermi level. The Fermi surface under a field, shown in Fig. 3(a), displays the importance of the additional bands crossing the Fermi level near $(\pm\pi, 0)$ and $(0, \pm\pi)$; the nesting vector that connects bands near the diagonals also leads to intraorbital nesting of the xy bands at the vHS, as denoted by the wavevector \vec{q} shown in Fig. 3(a).

To show this effect numerically, we perform self-consistent MF calculations using the interactions described in Eq. (1). The area of SDW order in 327 is shown in blue in Fig. 1, with an ordering wave vector $\vec{q} = (0.3\pi, 0)$, occurring between the field values of B_{c1} and B_{c2} , where $B_{c1} = 5.59 \times 10^{-3}$ and $B_{c2} = 8.43 \times 10^{-3}$ with μ_B set to 1, and B_{c1} corresponds to the field value at which the metamagnetic transition occurs. No SDW order is found in 214 or $(327)_0$ for the field values considered. Note that the vHS present in the single layer may lead to the formation of SDW order, however, this is significantly farther from the Fermi level than in 327, but is possibly related to the observations of SDW order in strained 214 [43], which remains to be investigated.

The SDW order parameters are shown in Fig. 3(b), where

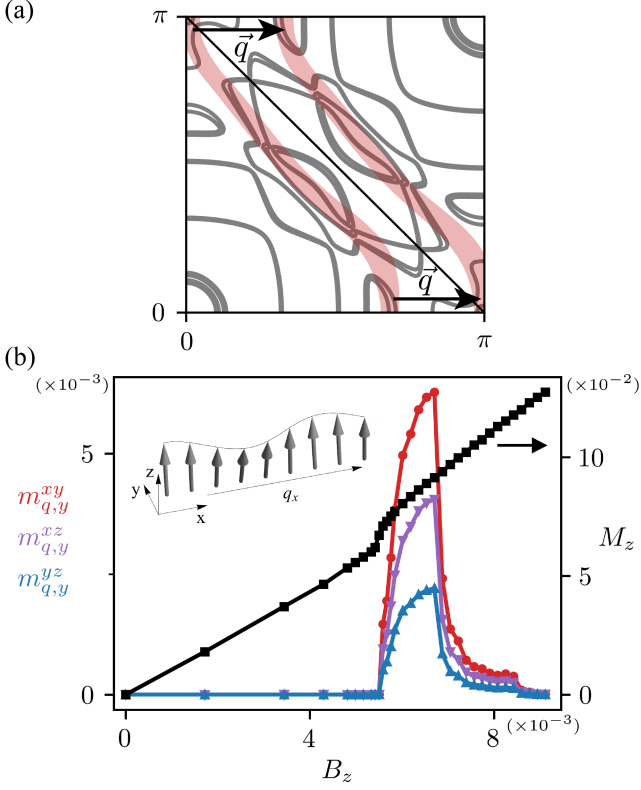


Figure 3. (a) Fermi surface in the presence of a small field slightly above B_c ($B_z = 6.02 \times 10^{-3}$) from TB parameters obtained through DFT calculations. The bands near $(\pm\pi, 0)$ and $(0, \pm\pi)$ occur by increasing the field, and are responsible for the increase in magnetization shown in (b). The red highlight shows some of the nesting that forms the SDW pairing. They lead to the SDW order under the same field that creates the metamagnetic transition. (b) Magnitude of the SDW order parameters, $m_{q,y}^a$, where a and y represent the orbital and magnetic moment direction, respectively, and M_z , the magnitude of the z magnetization. The inset shows a pictorial representation of the spins in the SDW state, with an overall magnetization in the z -direction from the field, and an oscillating y -component for an ordering wave vector \vec{q} in the x -direction.

the spin component is in the y -direction for the ordering in each of the three orbitals when the wave-vector is in the x -direction. The primary contribution comes from the xy orbital, and the next most significant contribution from the xz orbital. Note that a similar result is obtained when calculations are instead performed using an ordering wave vector in the y -direction, the SDW order occurs with spin in the x -direction, and the significant contributions come first from the xy orbital, then from the yz orbital. The region of finite SDW order begins at the field value where the magnetization also jumps, which corresponds to the field value at which the vHS reaches the Fermi level. Within this model of the bilayer, no SC regions are found.

Discussion and summary – The absence of SC in 327 must be considered when explaining potential superconducting states of 214 due to the similarity of the two materials. The most significant differences, the bilayer coupling and staggered rotations of oxygen octahedra, primarily af-

fects interorbital SC and therefore provides a natural explanation for the lack of SC in 327. The presence of SDW order in 327 under a field is another piece of the ruthenate puzzle. The Kanamori Hamiltonian provides a consistent framework for both SC and SDW order. The Hund’s coupling plays an important role in stabilizing interorbital SC, while the Hubbard repulsion and Hund’s coupling together lead to SDW order. This interaction is not enough on its own for ordering to form at zero field, but the increase in the DOS occurring in a field, experimentally observed as a metamagnetic transition, helps SDW ordering form. While the interactions presented here are limited to on-site, further neighbor interactions have been considered in interorbital SC studies of 214 [44]. The effect of these terms on SDW order remains to be studied, however, we do not expect additional interaction terms to qualitatively change the current theory.

Some limitations of our theory arise from the finite size of the TB model and MF approximation. Experiments detect multiple metamagnetic transitions and two SDW phases with different ordering wave vectors all separated by less than 1T [45]. Additionally, electron correlations beyond the MF approximation have been shown to be important in the formation of the heavy bands [46], which cannot be accounted for within MF theory. A larger TB model and inclusion of order parameter fluctuations may account for the flatness of the bands near the Fermi level, better reproducing the narrow range over which the metamagnetic transitions and SDW phases occur.

An area of recent development requiring consideration going forward is the possible SDW order observed in strained 214 [43]. While no experimental observations have been reported about the ordering wave vector or spin direction, this does appear to be a similar case to 327 since the SDW order again appears near a vHS. The shift of the vHS however, is instead induced by strain, so while the q_x and q_y ordered states are degenerate in the bilayer, only one of these is chosen by the uniaxial strain. Further work is required to fully differentiate the two cases. Other recent experiments have studied surface layers of 214 [47], and the trilayer, $\text{Sr}_4\text{Ru}_3\text{O}_{10}$ [48], both of which feature staggered rotations. No SC is found in the surface layers nor the trilayer, consistent with the current theory. However, future works are needed to estimate the surface effects including broken inversion symmetry.

In summary, we showed that interorbital SC provides a natural explanation for both the presence of SC in 214 and lack of SC in 327. In 327, the SC is destroyed by orbital hybridization introduced by staggered rotations of the octahedra, not present in 214. This same model finds intraorbital SDW ordering in 327 when the vHS is brought to the Fermi level via a magnetic field. We believe that the lack of SC in 327 is an important piece of the puzzle to determine the nature of the superconducting order in 214, and therefore interorbital SC should remain among the promising candidates. Additionally, we predict that ideal $(327)_0$, in which no rotations of the oxygen octahedra are present, can feature increased orbital degeneracy by tuning the bilayer coupling strength, and therefore can also

exhibit interorbital SC with a possibly higher transition temperature.

This work was supported by the Natural Sciences and Engineering Research Council of Canada Discovery Grant 06089-2016, and the Center for Quantum Materials at the University of Toronto. Computations were performed on the Niagara supercomputer at the SciNet HPC Consortium. SciNet is funded by: the Canada Foundation for Innovation under the auspices of Compute Canada; the Government of Ontario; Ontario Research Fund - Research Excellence; and the University of Toronto.

* hykee@physics.utoronto.ca

- [1] Y. Maeno, H. Hashimoto, K. Yoshida, S. Nishizaki, T. Fujita, J. G. Bednorz, and F. Lichtenberg, *Nature* **372**, 532 (1994).
- [2] A. P. Mackenzie and Y. Maeno, *Rev. Mod. Phys.* **75**, 657 (2003).
- [3] C. Kallin, *Reports on Progress in Physics* **75**, 042501 (2012).
- [4] A. P. Mackenzie, T. Scaffidi, C. W. Hicks, and Y. Maeno, *npj Quantum Materials* **2**, 40 (2017).
- [5] S. A. Kivelson, A. C. Yuan, B. Ramshaw, and R. Thomale, *npj Quantum Materials* **5**, 43 (2020).
- [6] R. S. Perry, L. M. Galvin, S. A. Grigera, L. Capogna, A. J. Schofield, A. P. Mackenzie, M. Chiao, S. R. Julian, S. I. Ikeda, S. Nakatsuji, Y. Maeno, and C. Pfleiderer, *Phys. Rev. Lett.* **86**, 2661 (2001).
- [7] S. A. Grigera, R. S. Perry, A. J. Schofield, M. Chiao, S. R. Julian, G. G. Lonzarich, S. I. Ikeda, Y. Maeno, A. J. Millis, and A. P. Mackenzie, *Science* **294**, 329 (2001).
- [8] R. S. Perry, K. Kitagawa, S. A. Grigera, R. A. Borzi, A. P. Mackenzie, K. Ishida, and Y. Maeno, *Phys. Rev. Lett.* **92**, 166602 (2004).
- [9] S. A. Grigera, P. Gegenwart, R. A. Borzi, F. Weickert, A. J. Schofield, R. S. Perry, T. Tayama, T. Sakakibara, Y. Maeno, A. G. Green, and A. P. Mackenzie, *Science* **306**, 1154 (2004).
- [10] K. Kitagawa, K. Ishida, R. S. Perry, T. Tayama, T. Sakakibara, and Y. Maeno, *Phys. Rev. Lett.* **95**, 127001 (2005).
- [11] R. A. Borzi, S. A. Grigera, J. Farrell, R. S. Perry, S. J. S. Lister, S. L. Lee, D. A. Tennant, Y. Maeno, and A. P. Mackenzie, *Science* **315**, 214 (2007).
- [12] A. Mackenzie, J. Bruin, R. Borzi, A. Rost, and S. Grigera, *Physica C: Superconductivity* **481**, 207 (2012), stripes and Electronic Liquid Crystals in Strongly Correlated Materials.
- [13] J. A. N. Bruin, H. Sakai, R. S. Perry, and A. P. Mackenzie, *Science* **339**, 804 (2013).
- [14] C. Lester, S. Ramos, R. S. Perry, T. P. Croft, R. I. Bewley, T. Guidi, P. Manuel, D. D. Khalyavin, E. M. Forgan, and S. M. Hayden, *Nature Materials* **14**, 373 (2015).
- [15] C. Lester, S. Ramos, R. S. Perry, T. P. Croft, M. Laver, R. I. Bewley, T. Guidi, A. Hiess, A. Wildes, E. M. Forgan, and S. M. Hayden, *Nature Communications* **12**, 5798 (2021).
- [16] T. M. Rice and M. Sigrist, *Journal of Physics: Condensed Matter* **7**, L643 (1995).
- [17] K. Ishida, H. Mukuda, Y. Kitaoka, K. Asayama, Z. Q. Mao, Y. Mori, and Y. Maeno, *Nature* **396**, 658 (1998).
- [18] A. Pustogow, Y. Luo, A. Chronister, Y.-S. Su, D. A. Sokolov, F. Jerzembeck, A. P. Mackenzie, C. W. Hicks, N. Kikugawa, S. Raghu, and et al., *Nature* **574**, 72 (2019).
- [19] A. Chronister, A. Pustogow, N. Kikugawa, D. A. Sokolov, F. Jerzembeck, C. W. Hicks, A. P. Mackenzie, E. D. Bauer, and S. E. Brown, *Proceedings of the National Academy of Sciences* **118** (2021), 10.1073/pnas.2025313118.
- [20] C. M. Puetter and H.-Y. Kee, *EPL (Europhysics Letters)* **98**, 27010 (2012).
- [21] S. Hoshino and P. Werner, *Phys. Rev. Lett.* **115**, 247001 (2015).
- [22] S. Hoshino and P. Werner, *Phys. Rev. B* **93**, 155161 (2016).
- [23] O. Gingras, R. Nourafkan, A.-M. S. Tremblay, and M. Côté, *Phys. Rev. Lett.* **123**, 217005 (2019).
- [24] H. G. Suh, H. Menke, P. M. R. Brydon, C. Timm, A. Ramires, and D. F. Agterberg, *Phys. Rev. Research* **2**, 032023 (2020).
- [25] A. W. Lindquist and H.-Y. Kee, *Phys. Rev. Research* **2**, 032055 (2020).
- [26] J. Clepkens, A. W. Lindquist, and H.-Y. Kee, *Phys. Rev. Research* **3**, 013001 (2021).
- [27] J. Clepkens, A. W. Lindquist, X. Liu, and H.-Y. Kee, *Phys. Rev. B* **104**, 104512 (2021).
- [28] A. Klejnberg and J. Spalek, *Journal of Physics: Condensed Matter* **11**, 6553 (1999).
- [29] X. Dai, Z. Fang, Y. Zhou, and F.-C. Zhang, *Phys. Rev. Lett.* **101**, 057008 (2008).
- [30] A. Ramires and M. Sigrist, *Phys. Rev. B* **94**, 104501 (2016).
- [31] O. Vafek and A. V. Chubukov, *Phys. Rev. Lett.* **118**, 087003 (2017).
- [32] A. K. C. Cheung and D. F. Agterberg, *Phys. Rev. B* **99**, 024516 (2019).
- [33] A. Ramires and M. Sigrist, *Phys. Rev. B* **100**, 104501 (2019).
- [34] S. Cobo, F. Ahn, I. Eremin, and A. Akbari, *Phys. Rev. B* **94**, 224507 (2016).
- [35] S. Raghu, A. Paramekanti, E. A. Kim, R. A. Borzi, S. A. Grigera, A. P. Mackenzie, and S. A. Kivelson, *Phys. Rev. B* **79**, 214402 (2009).
- [36] A. Tamai, M. P. Allan, J. F. Mercure, W. Meevasana, R. Dunkel, D. H. Lu, R. S. Perry, A. P. Mackenzie, D. J. Singh, Z.-X. Shen, and F. Baumberger, *Phys. Rev. Lett.* **101**, 026407 (2008).
- [37] H.-Y. Kee and Y. B. Kim, *Phys. Rev. B* **71**, 184402 (2005).
- [38] H. Yamase and A. A. Katanin, *Journal of the Physical Society of Japan* **76**, 073706 (2007).
- [39] W.-C. Lee and C. Wu, *Phys. Rev. B* **80**, 104438 (2009).
- [40] C. M. Puetter, J. G. Rau, and H.-Y. Kee, *Phys. Rev. B* **81**, 081105 (2010).
- [41] D. V. Efremov, A. Shtyk, A. W. Rost, C. Chamon, A. P. Mackenzie, and J. J. Betouras, *Phys. Rev. Lett.* **123**, 207202 (2019).
- [42] C. H. Mousatov, E. Berg, and S. A. Hartnoll, *Proceedings of the National Academy of Sciences* **117**, 2852 (2020).
- [43] V. Grinenko, S. Ghosh, R. Sarkar, J.-C. Orain, A. Nikitin, M. Elender, D. Das, Z. Guguchia, F. Brückner, M. E. Barber, J. Park, N. Kikugawa, D. A. Sokolov, J. S. Bobowski, T. Miyoshi, Y. Maeno, A. P. Mackenzie, H. Luetkens, C. W. Hicks, and H.-h. Klauss, *Nature Physics* , 1 (2021).
- [44] A. T. Rømer, P. J. Hirschfeld, and B. M. Andersen, *Phys. Rev. B* **104**, 064507 (2021).
- [45] Y. Tokiwa, M. Mchawat, R. S. Perry, and P. Gegenwart, *Phys. Rev. Lett.* **116**, 226402 (2016).
- [46] M. P. Allan, A. Tamai, E. Rozbicki, M. H. Fischer, J. Voss, P. D. C. King, W. Meevasana, S. Thirupathiah, E. Rienks, J. Fink, D. A. Tennant, R. S. Perry, J. F. Mercure, M. A. Wang, J. Lee, C. J. Fennie, E.-A. Kim, M. J. Lawler, K. M. Shen, A. P. Mackenzie, Z.-X. Shen, and F. Baumberger, *Phys. Rev. B* **15**, 063029 (2013).
- [47] C. A. Marques, L. C. Rhodes, R. Fittipaldi, V. Granata,

- C. M. Yim, R. Buzio, A. Gerbi, A. Vecchione, A. W. Rost, and P. Wahl, *Advanced Materials* **33**, 2100593 (2021).
- [48] G. Gebreyesus, P. Ngabonziza, J. Nagura, N. Seriani, O. Akin-Ojo, and R. M. Martin, (2021), [arXiv:2111.09591](https://arxiv.org/abs/2111.09591) [[cond-mat.str-el](https://arxiv.org/abs/2111.09591)].
- [49] G. Kresse and J. Hafner, *Phys. Rev. B* **47**, 558 (1993).
- [50] P. E. Blöchl, *Phys. Rev. B* **50**, 17953 (1994).
- [51] J. P. Perdew, K. Burke, and M. Ernzerhof, *Phys. Rev. Lett.* **77**, 3865 (1996).
- [52] A. A. Mostofi, J. R. Yates, G. Pizzi, Y.-S. Lee, I. Souza, D. Vanderbilt, and N. Marzari, *Computer Physics Communications* **185**, 2309 (2014).

Tight-binding model

To obtain tight-binding parameters, we perform density functional theory calculations with the Vienna *ab initio* simulation package (VASP) [49], using the projector augmented-wave potential [50] and the Perdew-Burke-Ernzerhof exchange-correlation functional [51], with an energy cutoff of 400 eV. The relevant TB parameters are obtained using WANNIER90 [52], and are listed in Tables I and II.

The TB model is given by,

$$\begin{aligned}
H_k = & \sum_{k,a,l} \xi_k^a c_{k,l,\sigma}^{a\dagger} c_{k,l,\sigma}^a + \sum_{k,l} t_k c_{k,l,\sigma}^{xz\dagger} c_{k,l,\sigma}^{yz} + \text{h.c.} \\
& + \sum_k t_{\perp}^{1D} (c_{k,t,\sigma}^{yz\dagger} c_{k,b,\sigma}^{yz} + c_{k,t,\sigma}^{xz\dagger} c_{k,b,\sigma}^{xz}) \\
& + t_{\perp}^{xy} c_{k,t,\sigma}^{xy\dagger} c_{k,b,\sigma}^{xy} - 2t_{\perp,x}^{xz} (c_{k,t,\sigma}^{yz\dagger} c_{k,b,\sigma}^{yz} \cos k_y \\
& + c_{k,t,\sigma}^{xz\dagger} c_{k,b,\sigma}^{xz} \cos k_x) - 2t_{\perp,x}^{xz/xy} (\sin k_y [c_{k,b,\sigma}^{xy\dagger} c_{k,t,\sigma}^{xz} \\
& - c_{k,t,\sigma}^{xy\dagger} c_{k,b,\sigma}^{xz}] + \sin_x [c_{k,b,\sigma}^{xy\dagger} c_{k,t,\sigma}^{yz} \\
& - c_{k,t,\sigma}^{xy\dagger} c_{k,b,\sigma}^{yz}]) + \text{h.c.} \\
& + \sum_k 2t^{\text{stag}} (\cos k_x + \cos k_y) (c_{k,t,\sigma}^{yz\dagger} c_{k+Q,t,\sigma}^{xz} \\
& - c_{k,t,\sigma}^{xz\dagger} c_{k+Q,t,\sigma}^{yz} - c_{k,b,\sigma}^{yz\dagger} c_{k+Q,b,\sigma}^{xz} \\
& + c_{k,b,\sigma}^{xz\dagger} c_{k+Q,b,\sigma}^{yz}) + \text{h.c.} \\
& + \sum_k t_{\perp}^{\text{stag}} (c_{k,t,\sigma}^{yz\dagger} c_{k+Q,b,\sigma}^{xz} - c_{k,t,\sigma}^{xz\dagger} c_{k+Q,b,\sigma}^{yz}).
\end{aligned} \tag{7}$$

Where $a \in (yz, xz, xy)$ represents the orbitals, and $l \in (t, b)$ is the layer index. The intraorbital dispersions are,

$$\begin{aligned}
\xi_k^{xz(yz)} = & -2t_x^{xz} \cos k_{x(y)} - 2t_y^{xz} \cos k_{y(x)} \\
& - 2t_{2x}^{xz} \cos 2k_{x(y)} - 2t_{3x}^{xz} \cos 3k_{x(y)} \\
& - 4t_{2x,y}^{xz} \cos 2k_{x(y)} \cos k_{y(x)} - \mu_{1D},
\end{aligned} \tag{8}$$

$$\begin{aligned}
\xi_k^{xy} = & -\mu_{xy} - \sum_n [2t_{nx}^{xy} (\cos nk_x + \cos nk_y) \\
& + 4t_{nx,ny}^{xy} \cos nk_x \cos nk_y] \\
& - \sum_{m \neq n} 4t_{mx,ny}^{xy} (\cos mk_x \cos nk_y \\
& + \cos nk_x \cos mk_y)
\end{aligned} \tag{9}$$

where m and n are the integers listed in Table II describing the intraorbital hopping within the xy orbitals between sites separated by $m\hat{x} + n\hat{y}$ as well as $n\hat{x} + m\hat{y}$ by symmetry. The dispersion of the xy orbital includes further neighbor hopping terms to model the flatness of the bands near $(\pm\pi, 0)$ and $(0, \pm\pi)$ of the Brillouin zone in the real bilayer material. The orbital mixing is given by,

$$t_k = -4t_{1D} \sin k_x \sin k_y. \tag{10}$$

The interlayer hoppings, t_{\perp}^{1D} and t_{\perp}^{xy} , represent hopping between layers within orbitals directly above or below each other, while $t_{\perp,x}^{xz}$ is hopping in the $xz(yz)$ orbital between

layers and one lattice site over in the $x(y)$ -direction, and $t_{\perp,y}^{xz/xy}$ hopping between layers, one lattice site over in the $y(x)$ -direction, between xy and $xz(yz)$ orbitals. The staggered hopping, t^{stag} , allowed by the staggered rotation, represents the hopping between NN $1D$ orbitals within a layer and changes sign between layers due to the opposite sense of the octahedra rotations between the layers, while t_{\perp}^{stag} occurs between $1D$ orbitals directly above or below each other. Finally, the SOC Hamiltonian is,

$$H_{\text{SOC}} = i\lambda \sum_i \sum_{abl} \epsilon_{abl} c_{i\sigma}^a \dagger c_{i\sigma'}^b \hat{\sigma}_{\sigma\sigma'}^l, \quad (11)$$

where the strength of the SOC used is set to $\lambda = 62.5$ meV throughout this work.

t_x^{xz}	t_y^{xz}	t_{2x}^{xz}	t_{3x}^{xz}	$t_{2x,y}^{xz}$
290.8	44.8	-47.0	-3.2	-13.5
t_x^{xy}	$t_{x,y}^{xy}$	t_{2x}^{xy}	$t_{2x,y}^{xy}$	$t_{2x,2y}^{xy}$
369.6	120.3	-4.2	20.3	14.1
t_{3x}^{xy}	$t_{3x,y}^{xy}$	$t_{3x,2y}^{xy}$	t_{4x}^{xy}	$t_{3x,3y}^{xy}$
4.8	4.4	5.5	1.9	4.0
$t_{4x,y}^{xy}$	$t_{4x,2y}^{xy}$	$t_{4x,3y}^{xy}$	t_{5x}^{xy}	$t_{5x,y}^{xy}$
2.6	3.1	2.9	x	x
μ_{xy}	t_{\perp}^{1D}	t_{\perp}^{xy}	$t_{\perp,x}^{xz}$	$t_{\perp,y}^{xz,xy}$
439.5	(290.8)	(44.8)	(120.3)	(10.1)
t^{stag}	t_{\perp}^{stag}	t_{1D}	μ_{1D}	
0	0	10.1	309.0	

TABLE I. Tight-binding parameters obtained for the single bilayer, 214, plus the additional bilayer coupling terms used to model the ideal bilayer, $(327)_0$, shown in parentheses. Note that the single layer and the ideal bilayer do not feature staggered rotations of the octahedra, so the staggered hopping terms are all 0 for both. Values that were not able to be obtained from DFT results are marked with an ‘x’. While these values are important when considering the vHS in the real bilayer, they are not expected to have any significant effect in the single layer since flat bands near the Fermi level are not present. All values are shown in units of meV. Values listed in the main text are all given in units of $2t_x^{xz} = 1$.

t_x^{xz}	t_y^{xz}	t_{2x}^{xz}	t_{3x}^{xz}	$t_{2x,y}^{xz}$
270.2	12.1	-29.8	-3.5	-10.1
t_x^{xy}	$t_{x,y}^{xy}$	t_{2x}^{xy}	$t_{2x,y}^{xy}$	$t_{2x,2y}^{xy}$
294.3	137.2	32.5	13.6	22.1
t_{3x}^{xy}	$t_{3x,y}^{xy}$	$t_{3x,2y}^{xy}$	t_{4x}^{xy}	$t_{3x,3y}^{xy}$
-12.5	10.3	1.34	8.99	2.2
$t_{4x,y}^{xy}$	$t_{4x,2y}^{xy}$	$t_{4x,3y}^{xy}$	t_{5x}^{xy}	$t_{5x,y}^{xy}$
-1.9	1.1	1.3	-3.76	0.7
μ_{xy}	t_{\perp}^{1D}	t_{\perp}^{xy}	$t_{\perp,x}^{xz}$	$t_{\perp,y}^{xz}$
402.2	281.6	18.6	90.6	13.6
t^{stag}	t_{\perp}^{stag}	t_{1D}	μ_{1D}	
84.5	64.3	12.6	284.4	

TABLE II. Tight-binding parameters obtained for the real bilayer, 327. All values are shown in units of meV. Note that the chemical potential listed here is slightly below a filling of $2/3$ to ensure that the vHS is close enough to the Fermi level to produce the metamagnetic transition at a field value near the experimentally observed 7.9 T. The chemical potential used corresponds to a filling fraction of approximately 0.657.

Intraorbital Superconductivity

To differentiate the effect of the bilayer on interorbital vs. intraorbital SC, we show the results for *intraorbital* SC. We study the effect of bilayer coupling in the TB model of the single layer with an attractive intraorbital s -wave interaction of the form,

$$H_s = -V \sum_a \phi_a^{\dagger} \phi_a, \quad (12)$$

where

$$\phi_a = \frac{1}{N} \sum_k c_{k,\sigma}^a [i\sigma_y]_{\sigma\sigma'} c_{-k,\sigma'}^a, \quad (13)$$

and $a \in (yz, xz, xy)$. The results of increasing t_{\perp} are summarized in Fig. 4. This shows that the orbital dependent bilayer terms have no effect on the SC for small values, while at larger values, the change in the gap size follows the same trend as the DOS near the Fermi level. Therefore, we conclude that the intraband pairing is not directly affected, but rather only feels secondary effects of the bilayer coupling due to the change in the DOS.

Since the change in the superconducting order parameter is only related to the DOS near the Fermi level, the addition of the bilayer coupling is not enough to justify the lack of SC in 327 within this model. Alternatively, recent work on interorbital SC has found that pairing can be negatively affected by orbital dependent hopping terms [26], as occurs for the bilayer coupling and the hoppings allowed by the staggered rotations.

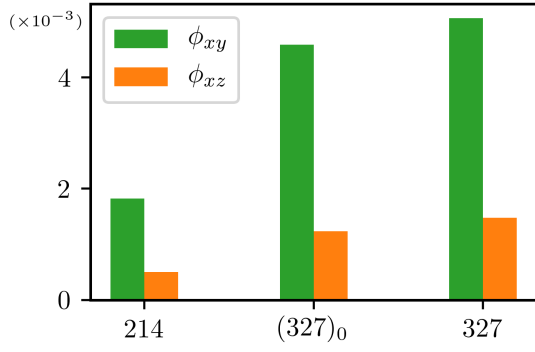


Figure 4. Size of the *intraorbital* SC order parameters given by Eq. 13 for the TB models of the single layer, ideal bilayer, and real bilayer, using an attractive *s*-wave interaction of $V = 0.2493$. Note that $\phi_{xz} = \phi_{yz}$. The superconducting order parameters increase with the DOS near the Fermi level, as the ideal and real bilayer models feature a DOS $1.20\times$ and $1.22\times$ greater than the single layer, respectively.